THE ASTROPHYSICAL JOURNAL, 494:657–673, 1998 February 20

A MULTITRANSITION CO AND CS (2–1) COMPARISON OF A STAR-FORMING AND A NON–STAR-FORMING GIANT MOLECULAR CLOUD

JONATHAN P. WILLIAMS
Harvard-Smithsonian Center for Astrophysics, 60 Garden Street, Cambridge, MA 02138; jpw@cfa.harvard.edu

AND

LEO BLITZ
Astronomy Department, University of California, Berkeley, Berkeley, CA 94720; blitz@gmc.berkeley.edu
Received 1997 June 5; accepted 1997 October 1

ABSTRACT

CO (3–2), CO (1–0), and CS (2–1) observations of clumps in the cold, low-luminosity cloud G216−2.5 discovered by Maddalena & Thaddeus are compared to the star-forming Rosette molecular cloud. The comparisons suggest that the clumps in a cloud may be characterized as being either dormant, incipient star forming, or star forming. In the Rosette molecular cloud, each set accounts for, respectively, 80%, 10%, and 10% of the total mass, but in G216−2.5, nearly 100% of the clumps are dormant. The physical conditions of the clumps in both clouds suggest a mass agglomeration evolutionary sequence from dormant to star-forming clumps.

Detailed results for the clumps in both clouds are as follows. Clump excitation conditions are remarkably uniform in G216−2.5 but show wide variation in the Rosette. CO (3–2) integrated intensities and the ratio of (3–2) to (1–0) emission are significantly greater in the star-forming cloud and greatest of all in those clumps with embedded *IRAS* sources. The ratio of CO (3–2) to (1–0) line widths is also greater in the Rosette cloud. Peak clump CO (1–0) temperatures are greater in the Rosette than G216−2.5, implying higher gas kinetic temperatures, and are highest of all for those clumps associated with *IRAS* sources. The ratios of peak CO (3–2) to (1–0) temperatures, however, are comparable in the two clouds, which implies that the volume density of emitting gas in the clumps in each cloud is similar, $n_{H_2} \simeq 10^3$ cm^{-3}. The CS observations indicate the presence of denser gas, $n_{H_2} \sim 10^5$ cm^{-3}, in the clumps in each cloud. CS integrated intensities are generally an order of magnitude weaker than ^{13}CO emission in each cloud, but the ratio of the two is a factor of 2 less in G216−2.5. CS to ^{13}CO line width ratios are also lower in G216−2.5, which suggests that there is a deficiency of dense gas relative to the Rosette. Again, the star-forming clumps in the Rosette possess the highest ratios. In addition, CO (2–1) emission was mapped over the central region of G216−2.5 and compared to a CO (1–0) map. The ratio of (2–1) to (1–0) integrated intensities increases toward the clump edges, which is opposite to the Sakamoto et al. study of the Orion molecular cloud. High-resolution ^{13}CO (2–1) maps of one clump in each cloud are compared to ^{13}CO (1–0) maps for evidence of further fragmentation. The (2–1) radial profile is steeper than the (1–0) profile in each clump but decreases at the same relative rate in the two clumps despite their different absolute sizes.

We conclude that the differences between clouds and clumps that are forming stars are most readily apparent in the warmer, denser gas traced by the CO (3–2) and CS (2–1) observations and note that there are two starless clumps in the Rosette molecular cloud with CO properties that are more characteristic of the star-forming clumps than the other starless clumps: these are the best candidates for the sites of future star formation in the cloud.

Subject headings: ISM: clouds — ISM: individual (G216−2.5, Rosette Molecular Complex) — ISM: molecules — ISM: structure — stars: formation

1. INTRODUCTION

In the study of a collection of objects, it is frequently the case that our understanding increases more by carefully studying one particularly unusual member of the group than by observing many normal ones. Molecular clouds in the Galaxy have been observed and mapped for more than two decades now, and, almost without exception, H II regions or infrared sources indicating recent star formation have been found to be associated with them. Generally, the more massive a cloud, the more massive the stars that form within it. However, a peculiar cloud discovered in an outer Galaxy survey by Maddalena & Thaddeus (1985) at $l \simeq 216°$, $b \simeq -2°.5$, and hereafter referred to as G216−2.5, is one of the largest and most massive clouds ($M = 3.4 \times 10^5\ M_\odot$) known in the solar neighborhood, yet it possesses no recognizable signs of OB star formation (Blitz 1993). Although there may be a small amount of low-mass star formation, the total infrared luminosity of the cloud is less than $2.4 \times 10^4\ L_\odot$ (Blitz 1990; Lee, Snell, & Dickman 1996). The luminosity-to-mass ratio, L_{IR}/M_{cloud}, which is a measure of the current star formation rate, is very low, $<0.07\ L_\odot/M_\odot$, compared to values of order unity for other clouds (Mooney & Solomon 1988; Scoville & Good 1989; Carpenter, Snell, & Schloerb 1990). G216−2.5, therefore, stands out as a most unusual member of that set of objects termed giant molecular clouds (GMCs) and, by the above reasoning, deserves attention.

Williams & Maddalena (1996) have found a large atomic photodissociation region to the north of G216−2.5 that shows that it appears to be physically associated with a

TABLE 1

CLOUD COMPARISON

Parameter	Rosette Molecular Cloud	G216−2.5
Mass (10^5 $M_\odot$)[a]	1.6	3.4
Projected area (pc^2)	2200	9400
CO line width (km s^{-1})	8.1	8.5
Mean column density (10^{21} cm^{-2})	6.6	3.3
Kinetic/gravitational energy	1.1	1.2
L_{IR}/M_{cloud} ($L_\odot/M_\odot$)	10	<0.07

[a] $N_{H_2}/W_{CO} = 2.3 \times 10^{20}$ cm^{-2}(K km $s^{-1})^{-1}$.

molecular cloud containing the S287 H II region. This may indicate that G216−2.5 is a remnant of a more massive, previously star-forming molecular complex. But since S287 is more than 50 pc distant, its current effect on G216−2.5 is negligible, and the two clouds are currently evolving independently of each other. Regardless of its previous history, G216−2.5 is currently dormant and is in a situation very different from most other GMCs for which star formation is observed to be more closely and directly associated with the molecular gas. No other similar cloud is known within 3 kpc of the Sun, a region containing dozens of giant molecular clouds.

In this paper, we compare CO (3–2) and CS (2–1) observations of G216−2.5 with the Rosette molecular cloud (hereafter RMC), which is in all respects a representative example of a GMC. The RMC is massive, $M = 1.6 \times 10^5$ $M_\odot$, and associated with both recent and current OB star formation (Blitz & Thaddeus 1980). The heating due to these stars results in an infrared luminosity that is more than 2 orders of magnitude greater than G216−2.5 (Blitz 1990; Cox, Deharveng, & Leene 1991). Table 1 directly compares global cloud properties for the two clouds and shows several interesting similarities and differences: G216−2.5 is more than twice the mass of the RMC, and its projected surface area is more than 4 times greater, yet the line widths of the two clouds are similar. Together these imply that the mean column density is a factor of 2 smaller in G216−2.5 than in the RMC but that the ratio of kinetic energy, $T = (3/2)M(\Delta v/2.355)^2$, to gravitational self-binding energy, $V = 3GM^2/5R$ (where G is the gravitational constant and an inverse square density profile is assumed), is similar and approximately equal to 1 (indicating equipartition but not virialization) in both clouds. In short, G216−2.5 may be described as a large, low surface brightness GMC lying in a shallow gravitational potential. The most striking entries in Table 1, however, are the values of L_{IR}/M_{cloud} for each cloud, lower in G216−2.5 by more than an order of magnitude. How is this related to the factor of 2 differences in the gas properties?

Williams, de Geus, & Blitz (1994) (hereafter Paper I) compared 0.7 pc scale resolution ^{13}CO (1–0) maps of the two clouds to see to what extent such large-scale differences are reflected in small-scale structure and dynamics. They found that the spectrum of fragmentation, as measured by the clump mass spectrum, mass size, mass line width, mass column density relation, etc., is very similar. The principal difference between the two maps is not so much their structure but their scale (Williams 1995), e.g., for any given mass, clumps in G216−2.5 have lower peak column densities and wider line widths than clumps in the RMC. At the parsec length scale and $\sim 10^3$ cm^{-3} density scale of these ^{13}CO observations, the star-forming nature of a clump is not readily apparent (Williams, Blitz, & Stark 1995; hereafter Paper II). Clearly, we must probe smaller length scales and higher density scales to find better indicators of the progress of a cloud or clump toward forming stars. We therefore began an observational study of $J > 1$ transitions of CO and CS (2–1) toward the centers of selected clumps in each cloud.

These observations are described in § 2, and the data are presented in § 3. Except for a CO (2–1) map of the central region of G216−2.5 in § 3.1, the observations of each cloud are complementary, and we defer the analysis and comparison of the two clouds to § 4. In that section, we perform a large velocity gradient analysis of the CO (3–2) to CO (1–0) ratio toward a number of clump peaks in each cloud and compare kinetic temperatures and densities. We also compare CO- and CS integrated intensities and line widths and ^{13}CO (1–0) and (2–1) profiles of a clump in each cloud, and we interpret the comparison in terms of a cloud evolutionary scenario. Our findings are summarized in § 5.

2. OBSERVATIONS

The data presented here were gathered over several observing runs at a number of sites, summarized in Table 2. Maps were made of small parts of G216−2.5, in the ^{13}CO (1–0), CO (1–0), and CO (2–1) lines. For the RMC, existing Bell Labs maps of ^{13}CO (1–0) and CO (1–0) were used (Blitz & Stark 1986). In addition, targeted observations toward the centers of a number of clumps in each cloud were made in CO (3–2), CS (2–1), and ^{13}CO (2–1).

Two regions toward the center of the G216−2.5 cloud were chosen from the original Columbia 1.2 m CO map of Maddalena & Thaddeus (1985) and were mapped in CO and ^{13}CO (1–0) during five observing runs on the NRAO[1] 12 m telescope from 1990 December to 1992 June. These observations were first described in Williams & Blitz (1993). The front end consisted of dual polarization SIS mixer receivers with total system temperatures in the range 250–500 K, and the back end consisted of two parallel filterbanks with frequency (velocity) resolutions of 100 kHz (0.26 km s^{-1}) and 250 kHz (0.65 km s^{-1}). The maps were made by standard ON-OFF-ON position switching from a reference position at $l = 216^\circ.0$, $b = -4^\circ.0$. Pointing was checked at the beginning, middle, and end of each observing session and found to be consistent within 10″. Overall calibration was checked daily using standard positions in the Rosette and Orion molecular clouds, and antenna temperatures are accurate to 15%. Scaling of the data between different observing runs was only necessary on the last run when a

[1] The National Radio Astronomy Observatory is operated by Associated Universities, Inc., under cooperative agreement with the National Science Foundation.

TABLE 2

SUMMARY OF OBSERVATIONS

Telescope	Line	Resolution	Description
NRAO 12 m	CO (1–0)	55″	Mapping of G216−2.5
	^{13}CO (1–0)	57″	Mapping of G216−2.5
	CS (2–1)	64″	Targeted pointings (G216−2.5 and RMC)
SEST 15 m	CO (3–2)	16″	G216−2.5 clumps 1, 12
	^{13}CO (2–1)	24″	G216−2.5 clump 1; RMC clump 2
Gornergrat 3 m	CO (3–2)	1′.2	Targeted pointings (G216−2.5 and RMC)
	CO (2–1)	1′.8	Mapping of G216−2.5 region 1
Bell Labs 7 m	CO (1–0)	1′.6	Mapping of RMC[a]
	^{13}CO (1–0)	1′.5	Mapping of RMC[a]

[a] Blitz & Stark 1986.

20% upward correction was made. Baselines were consistently flat, and a first-order fit was generally sufficient.

The locations of the two mapped regions are indicated on the Maddalena & Thaddeus (1985) map in Figure 1. The first was centered on the region of highest column density, and the second, about 1°.5 away, was selected at a more typical location in the cloud. Each map was full beamwidth (1′) sampled, corresponding to a linear resolution of 0.67 pc at a distance of 2.3 kpc (Williams & Maddalena 1996). This is about the same as the 1′.7 (0.79 pc) Bell Labs observations of the RMC by Blitz & Stark (1986), and therefore the spectra can be directly compared. From these ^{13}CO maps, the density structure in the two clouds was analyzed, and a catalog of clumps was defined (Paper I). Follow-up observations were then made directed at the center of a number of the clumps in each cloud.

CS (2–1) observations were made using the 12 m telescope in 1992 February. The setup was the same as for the above CO observations. Integration times varied from 5 to 10 minutes depending on signal strength and weather conditions. In this case, the linear resolution is different for the two clouds, and five-point crosses were observed at the clump peaks in the RMC so that the spectra cloud be smoothed to a coarser resolution for a fairer comparison with G216−2.5.

G216−2.5 was also partially mapped in the CO (2–1) line at the Gornergrat[2] 3 m telescope over a period of 30 days during 1990 September. The extent of the mapping is shown by the dashed line in Figure 1. The front end was a double sideband InP Schottky mixer receiver; typical single sideband system temperatures were 500 K. The back end was an acousto-optical spectrometer with 2048 channels and 32 kHz channel width corresponding to a velocity resolution at 230 GHz of 0.042 km s^{-1}. The observations were made by position switching with the same OFF position, $l = 216°.0$, $b = -4°.0$, as the NRAO 12 m data. Calibration was achieved by switching between warm and cold loads before each observation cycle, observing a standard position

[2] The Kölner Observatorium für Submillimeter und Millimeter Astronomie (KOSMA) 3 m radio telescope at Gornergrat-Süd Observatory is operated by the University of Cologne and supported by the Deutsche Forschungsgemeinschaft (DFG) through grant SFB 301, as well as special funding from the Land Nordrhein-Westfalen. The Observatory is administered by the Hochalpine Forschungsstationen Jungfraujoch und Gornergrat, Bern.

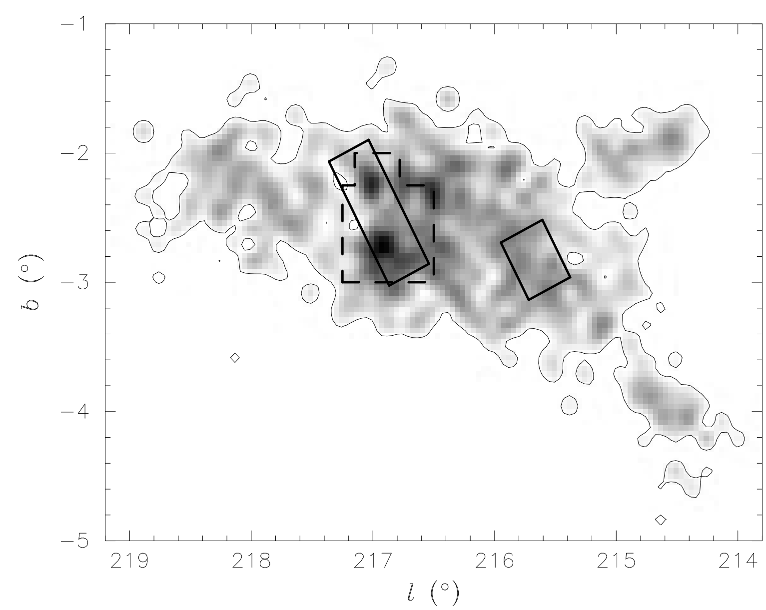

FIG. 1.—Location of observations overlaid on the Columbia 1.2 m map of velocity-integrated CO emission from Maddalena & Thaddeus (1985). The solid lines mark the area covered by the NRAO CO and ^{13}CO (1–0) observations: region 1 is the larger area at greater Galactic longitude. The dashed line marks the boundary of the Gornergrat CO (2–1) observations.

within G216−2.5 and the Orion molecular cloud (hereafter OMC) several times each day, and by skytips at the beginning and end of each observing run to measure the atmospheric opacity. The mapping was made in a regular grid with 2′ spacing, slightly greater than the telescope beam size of 1′.8. Antenna temperatures were corrected by the main beam efficiency of 0.58 and are T_R^* (Kutner & Ulich 1981). Third-order baselines were subtracted from the data, and channels were then averaged to attain a velocity resolution of 0.43 km s^{-1}. The typical root mean square (rms) noise level in the final spectra is 0.25 K per channel. We have used this map to investigate the spatial variation of the CO (2–1)/(1–0) ratio across the cloud in § 3.1 and clump line ratios in § 4.2.

CO (3–2) observations of G216−2.5 clumps 2, 3, and 4 (using the nomenclature of Paper I) and 12 positions in the RMC were made at the Gornergrat 3 m telescope in 1992 March. The observing mode for all the observations was position switching using reference positions $l = 216°.0$, $b = -4°.0$ for G216−2.5 and $l = 207°.6$, $b = -2°.2$ for the RMC. Calibration was checked by observing standard reference positions in each cloud and the OMC. Pointing was checked several times during each observing session by observing either planets or SiO masers in the OMC. As for the NRAO 12 m CS observations, 3 × 3 (five-point) crosses were made for each clump in the RMC, so that the resolution could be degraded to the larger beam of the Bell Labs ^{13}CO observations and to match the linear resolution of the more distant G216−2.5 cloud.

The 345 GHz receiver at the Gornergrat telescope was a double sideband InP Schottky. The back end was an acousto-optical spectrometer with 2048 channels and a 32 kHz (0.028 km s^{-1}) channel width for a total bandwidth of 65 MHz (57 km s^{-1}). System temperatures were typically 500 K (single sideband), and integration times on each point were generally 25 minutes. Spectral channels were averaged together to attain a velocity resolution of 0.11 km s^{-1}, and the rms noise per channel was typically about 0.1 K. Temperatures were converted by the main beam efficiency, $\eta_{\rm mb} = 0.40$, and are T_R^* (Kutner & Ulich 1981).

G216−2.5 clump 1 and RMC clump 2 were mapped in ^{13}CO (2–1) during an observing run at the Swedish-ESO Submillimeter Telescope (SEST) 15 m telescope in 1992 August. Limited CO (3–2) observations of G216−2.5 clumps 1 and 12 (which overlaps with 14) were also made. A description of the SEST telescope can be found in Booth et al. (1989). Observations were carried out over four days in 1992 August. The 345 GHz receiver was only available on the first day, and observations were performed using the 220 GHz receiver for the following three days. Both receivers had double sideband Schottky mixers. The back end in both cases was an acousto-optical spectrometer designed and built at the University of Cologne, which is very similar to the back end at the Gornergrat telescope. The frequency resolution was 50 kHz, and 2000 channels were available for a total bandwidth of 100 MHz. Typical single sideband system temperatures were 750 K at 345 GHz and 500 K at 220 GHz, and integration times per point were generally 15 and 10 minutes, respectively. Data were corrected for main beam efficiencies, $\eta_{\rm mb,345} = 0.25$ and $\eta_{\rm mb,220} = 0.54$, to place them on the T_R^* scale. Baselines (generally first order) were subtracted from the spectra and channels were then averaged together to attain a velocity resolution of 0.22 km s^{-1} and 0.12 km s^{-1}, respectively. Typical rms noise temperatures are 0.4 K for the CO (3–2) observations and 0.2 K for the ^{13}CO (2–1) spectra. A few SEST CO (3–2) pointings coincided with the Gornergrat observations, permitting a consistency check of the observing and data reduction techniques. In each case the spectra, when smoothed to the same spatial resolution, showed reasonable (20%) agreement.

The following sections concern themselves with the comparison of these observations between the two clouds. This is a fair and representative comparison, since the most massive clumps, $M > 10^3\ M_\odot$, were observed in each cloud.

3. RESULTS

3.1. *Gornergrat* CO (2–1) *Mapping*

Figure 1 shows the location of the Gornergrat CO (2–1) observations, and a map of the velocity-integrated emission is shown in Figure 2. There is a partial overlap with the CO (1–0) observations made at the NRAO 12 m telescope, and we have compared the ratio of integrated intensities in Figure 3. Here, the NRAO data has been smoothed to the same 2′ resolution as the Gornergrat data.

In each of the integrated intensity maps, two main condensations are clearly visible. These are not as apparent in the ratio map, which shows distinctly less contrast, indicating that there are no large variations of density, optical depth, or kinetic temperature at the clump surfaces. Judging from the strength of the ^{13}CO emission, both CO lines are optically thick, so for thermalized emission at a kinetic temperature of $T_{\rm kin} \gtrsim h\nu_{21}/k = 11$ K, the ratio of integrated intensities should be unity. The observed value is generally less than one and implies either low gas densities, $n_{\rm H_2} < 10^3$ cm^{-3}, and/or low kinetic temperatures $T_{\rm kin} \lesssim 10$ K, either of which would result in the $J = 2$ level being underpopulated.

Ratios less than one are also observed in the OMC (Sakamoto et al. 1994), but they tend to be seen on the periphery of the cloud away from the main ridge. The principal difference between the two clouds is how the ratio correlates with the emission. In the OMC, the larger line ratios are seen toward the center of the main ridge, whereas in G216−2.5, they are seen toward the clump edges. This is evident from the maps in Figure 3, but it is also shown graphically in Figure 4. This behavior could be explained by higher peak densities in both the clump and interclump gas in the OMC. Higher peak clump densities in the OMC drive the (2–1)/(1–0) line ratio toward the optically thick thermalized limit, whereas lower interclump densities but still optically thick gas would lower the ratio toward clump edges and in interclump gas. In G216−2.5, if the peak clump densities are less than that in the Orion clumps, the centers might only show the line ratios in the subthermal optically thick regime, and toward the clump edges, the ratios may rise because the lines are becoming optically thin.

3.2. CO (3–2) *Spectra*

Five positions (see Table 3) centered on ^{13}CO clump peaks in G216−2.5 were observed in the CO (3–2) line. Their locations with respect to the cloud are indicated on the ^{13}CO NRAO map in Figure 5, where the clump numbers follow the nomenclature of Table 3A in Paper I. Spectra of the three lowest transitions of CO and ^{13}CO (1–0) are shown in Figure 6. CO temperature ratios are computed across the line wherever the signal-to-noise ratio

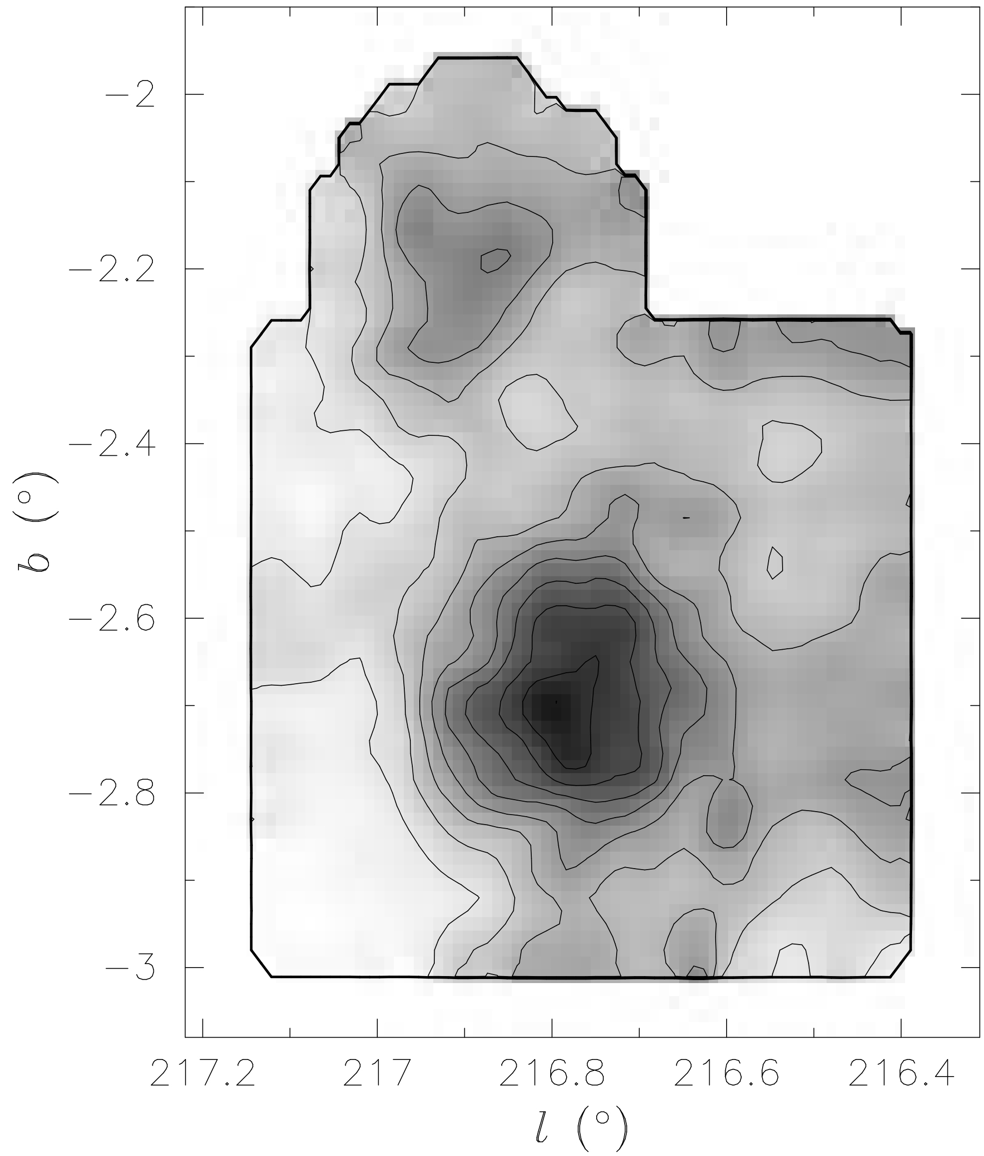

FIG. 2.—Velocity-integrated CO (2–1) emission toward the central region of G216−2.5. Spectra were taken at the Gornergrat 3 m telescope at full beamwidth (2′) separation and have been integrated from 17 to 30 km s^{-1}. Contour levels are at $4n$ K km s^{-1} ($n = 1, 2, 3, \ldots$).

is sufficiently high (after first rebinning spectra to a common velocity scale and resolution).

Clumps 1 to 4 are in the same region of the cloud, which is a large central condensation prominent in the original Maddalena & Thaddeus (1985) map. All four clumps have quite similar spectra, in ^{13}CO (1–0) and the three transitions of CO, suggesting remarkably uniform physical conditions of the gas despite the inhomogeneities in the cloud. Clumps 12 and 14 are at different velocities along a single line of sight separated from clumps 1 to 4 by about 20′ (14 pc projected distance). Line ratios are lower here, but the peak CO brightness temperature for clump 12, at least, is the same as for clumps 1–4, which suggests that the lower ratios are due to lower densities.

TABLE 3

G216L − 2.5 POINTING CENTERS

Clumps	Δα[a]	Δδ[b]	$M_{\rm LTE}$ ($M_\odot$)[c]	$M_{\rm grav}/M_{\rm LTE}$[c]
1	−5′	−2′	499	2.39
2	−2	2	738	1.71
3	−9	−4	894	3.78
4	−2	−1	516	3.64
12/14......	20	2	57/184	8.10/7.00

[a] Offset from α(1950) = 6$^{\rm h}$46$^{\rm m}$50$^{\rm s}$.
[b] Offset from δ(1950) = −4°31′14″.
[c] $d = 2300$ pc, $N_{\rm H_2}/N_{\rm CO13} = 5 \times 10^5$.

Twelve positions (see Table 4), also centered on ^{13}CO clump peaks, were observed in the RMC. Their positions are indicated on the CO (1–0) Bell Labs map of Blitz & Stark (1986) in Figure 7: here clump numbers follow the nomenclature of Table 2 in Paper II. Spectra of CO (1–0), CO (3–2), their ratio, and ^{13}CO (1–0) are shown in Figure 8. Immediately apparent is the greater range both of line strengths and line ratios in the RMC compared to G216−2.5, which implies a greater diversity in physical conditions in the clumps. In both clouds, the spectra are from the largest, brightest clumps in the cloud. We discuss this further in § 4. Along several lines of sight, there is more than one velocity component present in the ^{13}CO spectrum

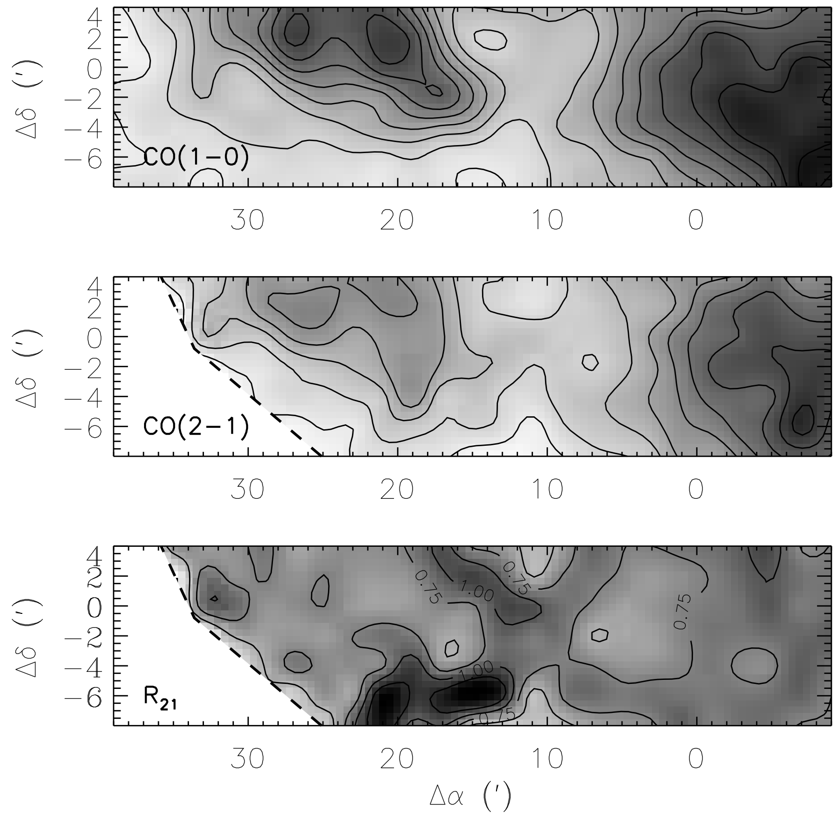

FIG. 3.—Integrated CO (2–1) and CO (1–0) emission and their ratio in the region where the two sets of observations overlap in Fig. 1. The map center is at $\alpha(1950) = 6^h46^m50^s$, $\delta(1950) = -4°31'14''$. The top panel shows NRAO 12 m CO (1–0) data smoothed to a resolution of 2′ and integrated over the velocity range $v = 15$–35 km s^{-1}. Contours begin at and increment 4 K km s^{-1}. The middle panel shows the Gornergrat 3 m CO (2–1) data at the same resolution, integrated over the same velocity range, and at the same contour levels. The boundary of these observations is indicated by the dashed line. The bottom panel is the ratio of integrated CO (2–1) to CO (1–0) intensities, with contours at 0.5, 0.75, 1.0, and 1.25.

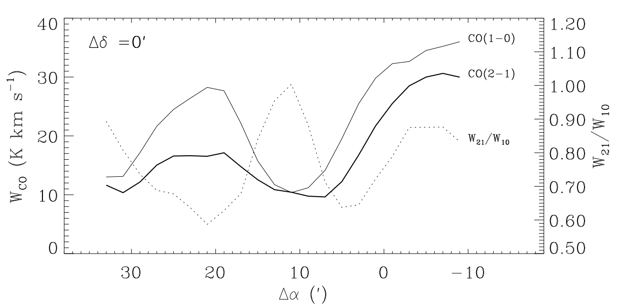

FIG. 4.—Variation of the integrated intensities of CO (2–1) and CO (1–0) and their ratio along $\Delta\delta = 0$ ($\delta[1950] = -4°31'14''$). Each cross section has been Gaussian smoothed to 3′ resolution.

that, in three cases, can be unambiguously identified with another cataloged clump. These are indicated in the appropriate figure: the spectrum toward clump 1 contains a component from clump 6, clump 5 contains a component from clump 21, and clumps 8 and 14 both contain a component from clump 17.

The dip in the CO spectra at the peak of the ^{13}CO spectrum shows that there is strong self-absorption toward clump 2. There also appears to be similar, but weaker, self-absorption toward clumps 4 and 6, and therefore these three clumps are not included in the large velocity gradient (LVG) analysis of the CO (3–2) to (1–0) line ratio. There is also one case (clump 24) where an abnormally high

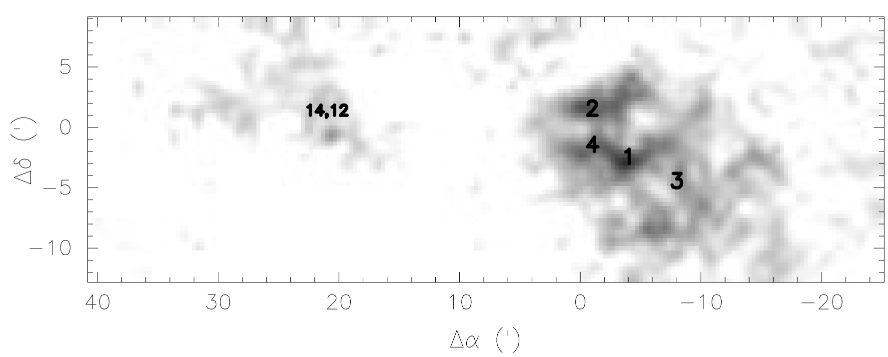

FIG. 5.—Location of the observed clumps in G216−2.5. The gray-scale image is a velocity-integrated map of ^{13}CO (1–0) emission. Clump numbers correspond to Table 3A in Williams et al. (1994). The map center is $\alpha(1950) = 6^h46^m50^s$, $\delta(1950) = -4°31'14''$.

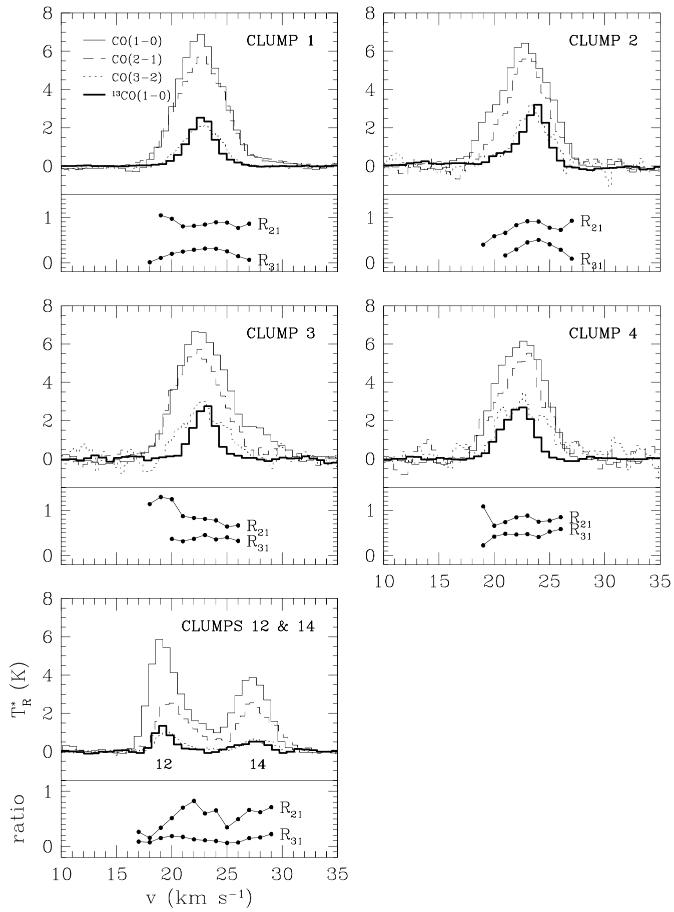

FIG. 6.—The ^{13}CO (1–0), CO (1–0), (2–1), and (3–2) spectra and their ratio for the observed clumps in G216−2.5. The ratios were calculated by rebinning the spectra to a common velocity scale and resolution, indicated by circles.

TABLE 4

ROSETTE MOLECULAR CLOUD POINTING CENTERS

Clumps	l	b	$M_{\rm LTE}$ $(M_\odot)^{\rm a}$	$M_{\rm grav}/M_{\rm LTE}{}^{\rm a}$
1[b]	207°.015	−1°.823	2532	0.27
2[b]	207.265	−1.823	2417	0.48
3[b]	207.565	−1.723	2373	0.66
4	207.790	−1.773	2035	0.36
5/21	207.715	−1.923	1700/337	0.59/0.78
6	207.115	−1.848	1540	0.43
7[b]	207.290	−2.148	1175	0.38
8/17	207.140	−1.898	1059/467	0.39/0.78
12	207.365	−1.448	727	1.02
14/17......	207.115	−1.873	657/467	0.91/0.78S
20	207.240	−1.573	372	2.60
24	207.915	−1.798	294	0.88

[a] $d = 1600$pc, $N_{\rm H_2}/N_{^{13}\rm CO} = 5 \times 10^5$.
[b] Contains *IRAS* source.

CO/^{13}CO ratio is observed at a distinct velocity away from the main clump. This is also seen in a number of spectra toward G216−2.5, and it indicates low CO line opacities. Because of the low column density and scarcity of such features, however, such gas contributes little to the total mass of the complex as a whole.

Of the observed clumps in the RMC, numbers 1, 2, 3, and 7 have associated *IRAS* sources (Paper II). There is an *IRAS* source toward clump 5 also, but it is faint toward the edge of the clump, and follow-up, near-infrared mapping by Phelps & Lada (1997) failed to find any embedded stars toward the clump center. For this paper, therefore, we do not consider clump 5 to be an active star-forming clump in the same category as clumps 1, 2, 3, and 7.

3.3. CS *Spectra*

CS (2–1) and ^{13}CO (1–0) spectra are plotted for each clump in the two clouds in Figures 9 and 10. The ^{13}CO line is shown here rather than the CO line because its optical depth is much lower, and the CO shows self-absorption in a number of clumps in the RMC. To allow for the closer distance of the RMC, the resolution of the CS spectra has been degraded by making weighted averages of 3 × 3 crosses about the center position, with the result that the effective resolution is close to that of the 1′.7 resolution of the Bell Labs ^{13}CO observations, and the linear resolution, 0.7 pc, the same as for G216−2.5.

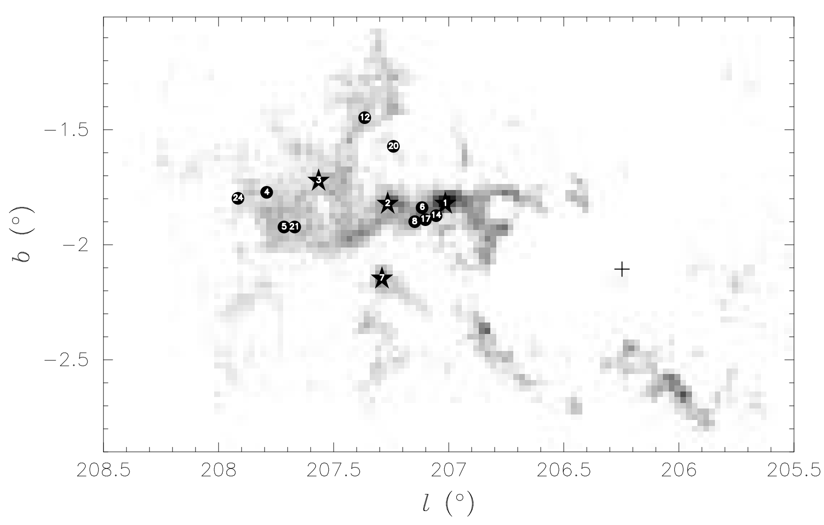

FIG. 7.—Location of the observed clumps in the RMC. The gray-scale image is a velocity-integrated map of ^{13}CO (1–0) emission. Clump numbers correspond to Table 2 in Williams et al. (1995). The clumps with embedded *IRAS* sources are indicated with stars. The cross marks the center of the OB association, NGC 2244, that powers the Rosette Nebula.

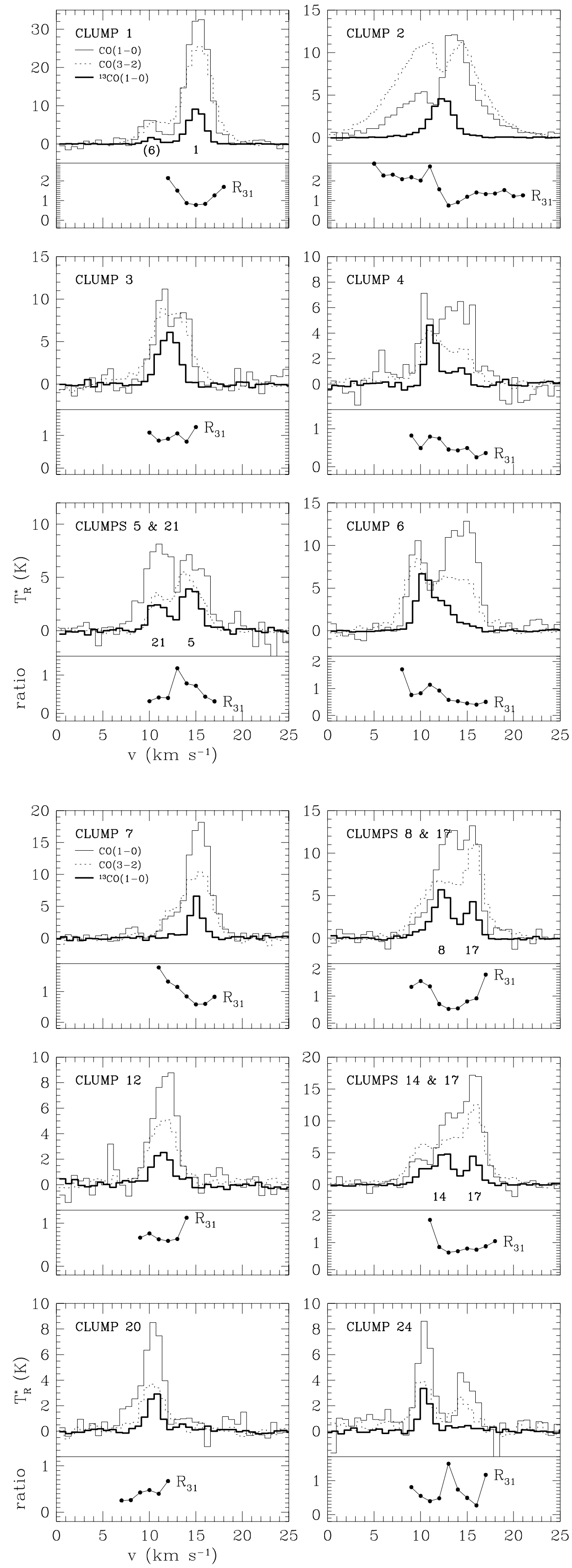

FIG. 8.—The ^{13}CO (1–0), CO (1–0), and (3–2) spectra and their ratio for the observed clumps in the RMC. The ratios were calculated by rebinning the spectra to a common velocity scale and resolution, indicated by circles.

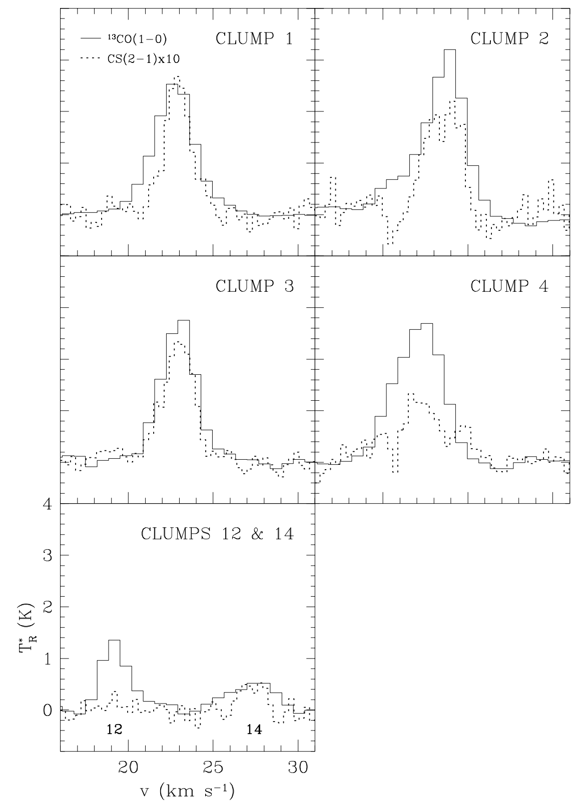

FIG. 9.—CS (2–1) and ^{13}CO (1–0) spectra toward a number of clumps in G216−2.5. Both sets of data were taken at the NRAO 12 m telescope and are at very nearly the same resolution. The velocity and temperature axes are indicated in the bottom, left-hand panel. For purposes of comparison, the CS emission (*dotted line*) has been multiplied by a factor of 10.

The CS emission is generally very weak, and the spectra in Figures 9 and 10 have been shown multiplied by a factor of 10 for comparison. Observations were made for a sufficient time to achieve a similar signal-to-noise ratio as the ^{13}CO spectra. Inspection of the figures show that CS and ^{13}CO line profiles are remarkably similar in many cases; we compare line widths and integrated intensities in § 4.3.

3.4. *Clump Substructure*

The structure that is ubiquitously observed in parsec-scale resolution ^{13}CO maps of molecular clouds is only the first step in a fragmentation process that ends in individual, dense, star-forming cores. For example, each clump with an embedded *IRAS* source in the RMC contains a small cluster of stars (Phelps & Lada 1997), and so further fragmentation to much smaller scales must have taken place at some time. Moreover, a number of clumps in the RMC are gravitationally bound and may, therefore, be considered a distinct physical unit that might evolve structures in a similar manner to the gravitationally bound cloud of which they are a part. Can observations at higher resolution reveal such clump substructure?

To address this question, we mapped one clump in each cloud in the (2–1) line of ^{13}CO with the SEST 15 m telescope. The resolution of these maps is 24″, which is greater than corresponding (1–0) maps by a factor of more than 2 for G216−2.5 and close to a factor of 4 for the RMC. In addition, the critical density of the (2–1) line is greater than that of the (1–0) line (by a factor of 8 if optically thin), and so

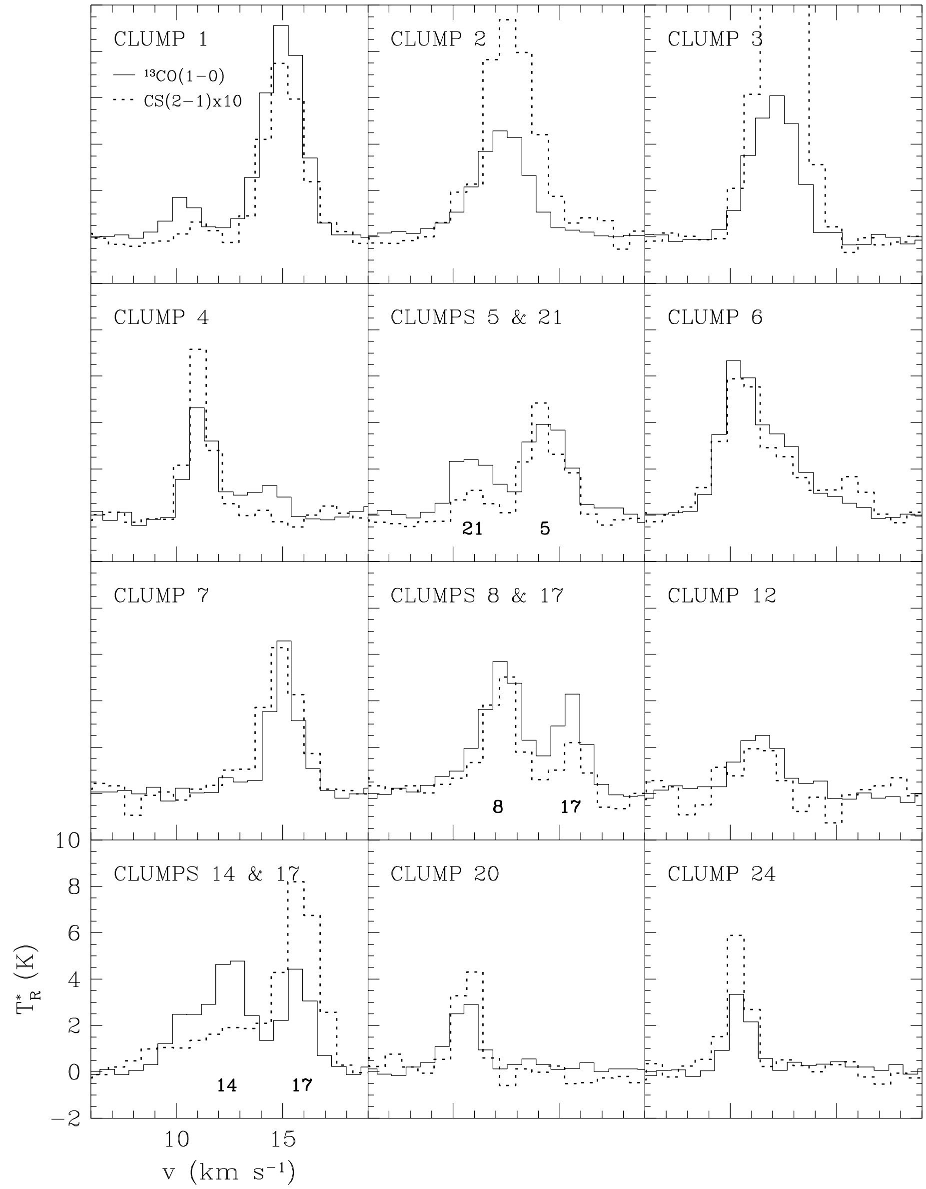

FIG. 10.—As Fig. 9, but for clumps in the RMC. The ^{13}CO data is from the Bell Labs 7 m telescope, and the CS from observations at the NRAO 12 m telescope. The CS spectra presented here are an average of a 3 × 3 cross so as to have an effective resolution close to that of the ^{13}CO spectra and the G216−2.5 data.

the resulting maps are sensitive to smaller features and greater densities than the (1–0) maps.

3.4.1. *G216−2.5 Clump 1*

Clump 1 in G216−2.5 contains the strongest observed CO (1–0) line in the cloud ($T_{\rm peak}$ = 6.8 K). SEST ^{13}CO (2–1) and NRAO velocity-integrated ^{13}CO (1–0) maps are overlaid in Figure 11. A small extension of the main peak to the south at $\Delta\alpha = -4\rlap{.}'3$, $\Delta\delta = -3'$ is visible in the (2–1) map. However, in position-velocity cuts through the center of the clump (Figs. 12 and 13), the (2–1) and (1–0) contours follow each other closely, and no new structure is evident. The cut shown in Figure 14, made along the small extension shown in Figure 11, shows some breaking up of the clump into two fragments. However, the separation between these fragments occurs at the same velocity, and it is therefore unclear whether the figure is showing excitation or density variations within the clump. At the 0.27 pc resolution of the (2–1) observations and the densities, $n_{\rm H_2} \sim 10^3$ cm^{-3}, traced by them, there is little unambiguous evidence for substructure.

3.4.2. *RMC Clump 2*

Clump 2 in the RMC contains the infrared source GL 961 (Cohen 1973). The CO (1–0) and (3–2) spectra are both strongly self-absorbed and have very broad line wings, considerably larger than the ^{13}CO line width (Fig. 8) owing to an optically thick core and an optically thin outflow (Blitz & Thaddeus 1980; Lada & Gautier 1982). SEST and Bell Labs maps are presented in Figures 15, 16, and 17. At the distance of the RMC, the (2–1) map resolution is 0.19 pc, which is substantially higher than the 0.7 pc resolution of the (1–0) map. Nevertheless, the velocity-integrated map does not show any clear substructure; the clump is more centrally condensed (see § 4.4) and better defined in the (2–1)

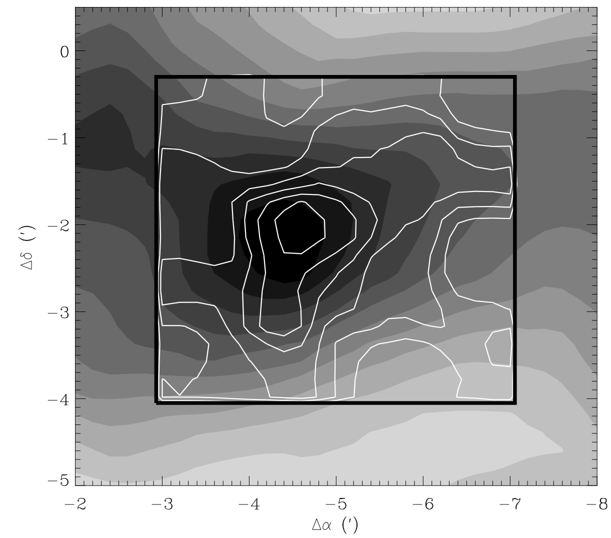

FIG. 11.—Velocity-integrated map of NRAO 12 m ^{13}CO (1–0) and SEST 15 m ^{13}CO (2–1) emission in G216−2.5 clump 1. Offsets are relative to the map center of region 1, $\alpha(1950) = 6^h46^m50^s$, $\delta(1950) = -4°31'14''$. Both lines have been integrated over $v = 20$ to 25 km s^{-1}, and the (1–0) emission is shown as a halftone from 3.5 to 9 K km s^{-1}. The (2–1) emission is shown in contours starting at 2 K km s^{-1} at steps of 0.5 K km s^{-1}. The boundary of the SEST observations is indicated by the heavy, black line.

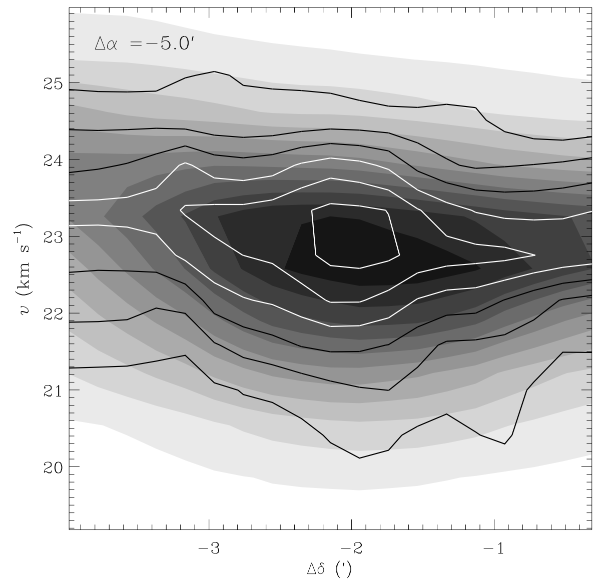

FIG. 13.—The $\Delta\delta - v$ map of ^{13}CO (1–0) and (2–1) emission in G216−2.5 clump 1 at $\Delta\alpha = -5'$. Halftone and contour levels are as in Fig. 12.

map than in the (1–0) map. There is a small ($\simeq 40''$) offset between the peaks of the two maps whose origin is unknown, but it may be due to optical depth effects: the CO emission is clearly very saturated, and it is quite possible that the ^{13}CO emission is also optically thick, or nearly so, especially at the clump center. In this case, the two maps may not show the total column density through the clump but the kinetic temperature at different depths within it. The position-velocity diagrams (Figs. 16 and 17) show two features at the highest contour levels, but it is unclear whether this substructure is due to true density variations or line saturation effects in this complex clump.

Our search for substructure is therefore inconclusive. Although some substructure may be evident in G216−2.5 clump 1, the small increase in resolution of the (2–1) over the 1–0 observations does not permit us to draw any strong conclusions. In the case of RMC clump 2, although our (2–1) observations have about 4 times the resolution of the (1–0) data, we still cannot be certain that true density substructure had been identified; higher resolution observations of more optically thin, high-density tracers are required. With the caveat that we have only looked at two

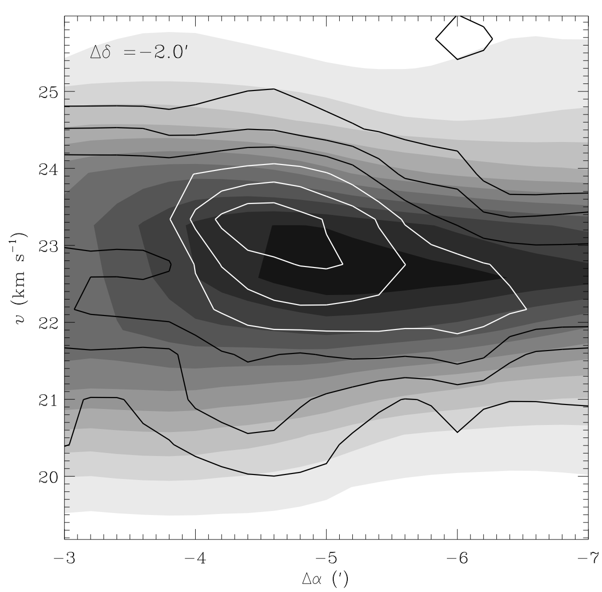

FIG. 12.—The $\Delta\alpha - v$ map of ^{13}CO (1–0) and (2–1) emission in G216−2.5 clump 1 at $\Delta\delta = -2'$. The (1–0) map is again shown in halftone, from 0.25 to 4 K, and the (2–1) map in contours at 0.25n K ($n = 1, 2, 3, \ldots$).

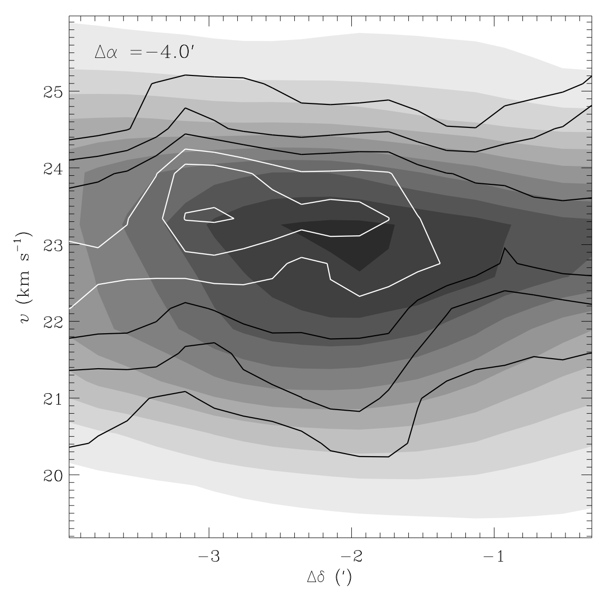

FIG. 14.—The $\Delta\delta - v$ map of ^{13}CO (1–0) and (2–1) emission in G216−2.5 clump 1 at $\Delta\alpha = -4'$. Halftone and contour levels are as in Fig. 12.

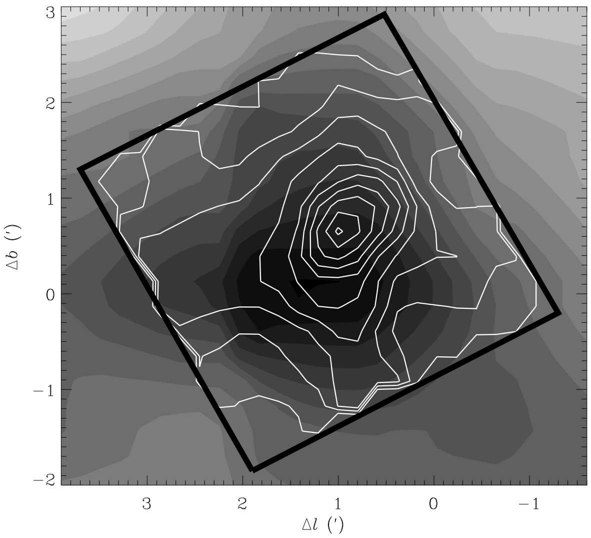

FIG. 15.—Velocity-integrated map of Bell Labs 7 m ^{13}CO (1–0) and SEST 15 m (2–1) emission in RMC clump 2. The map center is $l = 207°.250$, $b = -1°.823$. Both lines have been integrated over $v = 8$ to 18 km s^{-1}, and the (1–0) emission is shown as a halftone from 3 to 21 K km s^{-1}. The (2–1) emission is shown in contours starting at 7.5 K km s^{-1}, in steps of 1.5 K km s^{-1}. The boundary of the SEST observations is indicated by the heavy, black line.

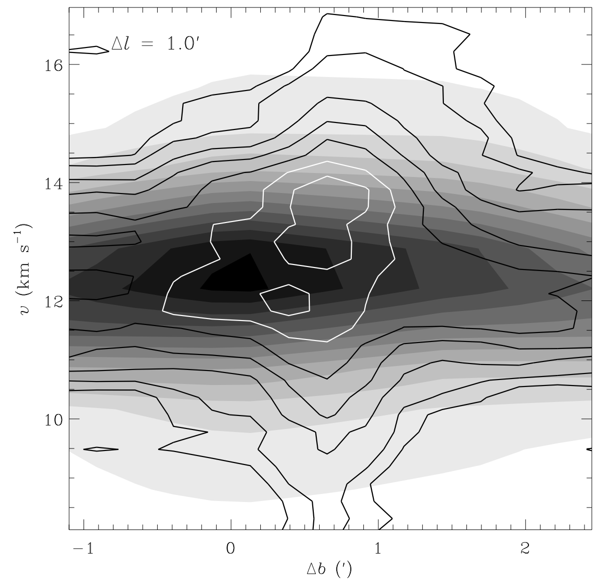

FIG. 17.—A $b - v$ map of ^{13}CO (1–0) and (2–1) emission in RMC clump 2 at $\Delta l = 1°.0$. The (1–0) data is shown in halftone, from 0.5 to 6 K, and the (2–1) map in contours at $0.5n$ K ($n = 1.5, 2, 3, 4, \ldots$).

clumps, one in each cloud, it appears that millimeter interferometric observations are required to achieve the resolution necessary to determine whether or not and on what scale significant substructure exists in the resolved clumps.

4. ANALYSIS AND COMPARISON OF THE TWO CLOUDS

In this section, we analyze and compare the data from the two clouds. The masses of the most massive G216−2.5 clumps are more than a factor of 2 less than the most massive clumps in the RMC (Tables 3 and 4), and to take this into account, we have divided up the set of RMC clumps into three groups based on their mass, their degree of gravitational boundness, and whether or not they contain embedded stars. Following Paper II, we take the ratio $\alpha = M_{\rm grav}/M = 3R\sigma_v^2/2GM$ to be the measure of gravitational boundness, which is 1.0 for marginally bound clumps and 0.5 for virialized clumps.

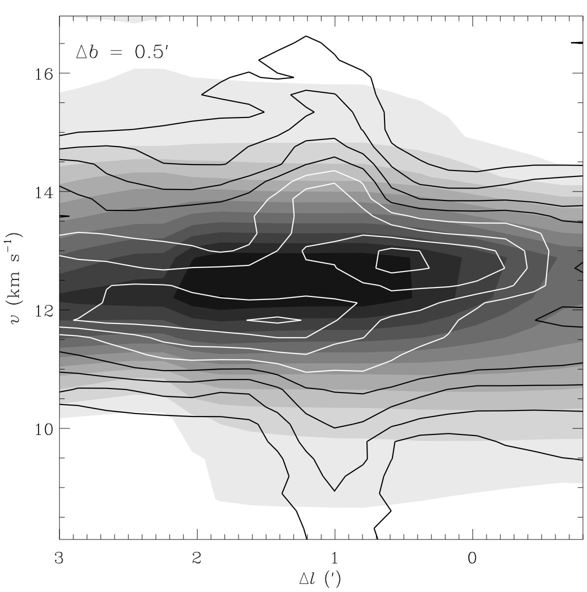

FIG. 16.—A $l - v$ map of ^{13}CO (1–0) and (2–1) emission in RMC clump 2 at $\Delta b = 0°.5$. The (1–0) data is shown in halftone, from 0.5 to 6 K, and the (2–1) map in contours at $0.5n$ K ($n = 1, 2, 3, \ldots$).

Group 1 (clumps 1, 2, 3, and 7) comprises the most massive clumps, $\langle M \rangle = 2124\ M_\odot$, and each has an associated *IRAS* source. These clumps are strongly self-gravitating, with $\langle \alpha \rangle = 0.45$ (see Paper II for a discussion of values of $\alpha < 0.5$). Group 1 consists of the clumps with active star formation.

Group 2 (clumps 4, 5, 6, and 8) comprises clumps that are also strongly self-gravitating with $\langle \alpha \rangle = 0.44$ but have no embedded *IRAS* sources. The group 2 clumps are somewhat less massive than those in group 1, with $\langle M \rangle = 1584\ M_\odot$. Because the clumps in this group are nearly as massive and as tightly bound as those in group 1, they are the prime candidates for the sites of future star formation in the cloud, and therefore we refer to them as incipient star-forming clumps.

Group 3 consists of clumps 12, 14, 17, 20, 21, and 24; they contain no stars and are, on average, only marginally gravitationally bound with $\langle \alpha \rangle = 1.16$ and a mean mass, $\langle M \rangle = 476\ M_\odot$, comparable to clumps 1–4 in G216−2.5. We call these loosely bound clumps dormant because they are unlikely, in their present state, to ever form stars.

We will primarily compare group 3 in the RMC with clumps 1–4 in G216−2.5 as a measure of the difference between the two clouds because of their similarity in mass. We note, however, that clumps 1–4 in G216−2.5 are much less tightly bound ($\langle \alpha \rangle = 2.88$; Paper I) than those in group 3 in the RMC and are therefore not even self-gravitating. We use the comparison of group 1 with group 2 as a measure of the difference between the star-forming and non–star-forming clumps in the RMC. Clumps 1–4 in G216−2.5 may, of course, be compared with groups 1 and 2, or the ensemble of all clumps in the RMC, but the differ-

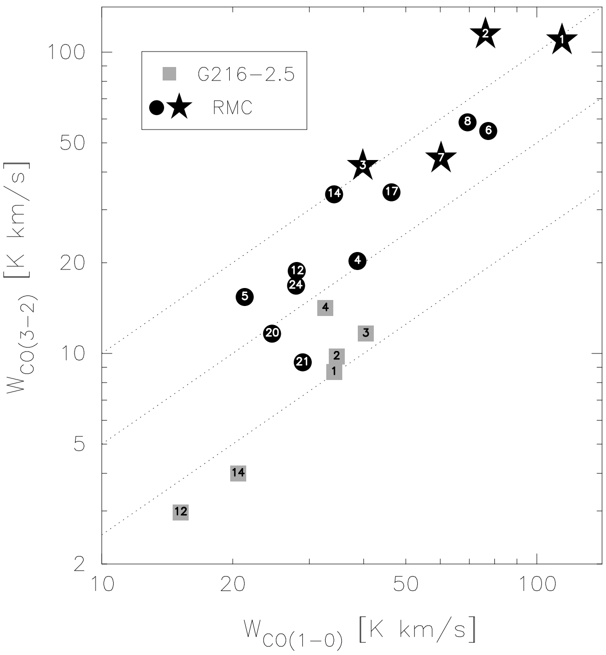

FIG. 18.—Comparison of CO (1–0) and (3–2) peak integrated intensities for clumps in the two clouds. The squares are clumps in G216−2.5, circles are clumps in the RMC, and the stars are those clumps in the RMC with embedded *IRAS* sources. The numbers correspond to the spectra in Figs. 6 and 8, respectively. The dotted lines are at $W_{CO\,(3-2)}/W_{CO\,(1-0)} = 1$, 0.5, 0.25. Clumps in G216−2.5 have both lower CO peak integrated intensities and smaller (3–2)/(1–0) ratios than clumps in the RMC. The ratio tends to be highest in the *IRAS* clumps.

ences would be more extreme and only strengthen the conclusions that we draw from the comparison with the low-mass clumps in group 3.

4.1. CO (3–2) *Comparison*

Integrated intensities of CO (1–0) and CO (3–2) are plotted against each other in Figure 18. In most cases, the spectra are not blended with other structures in the cloud, and integrated intensities are calculated by simply summing over the channels for which there is signal. There are some clumps in the RMC, however, that are blended together. In these cases, integrated intensities are calculated by bisecting the spectra at the velocity of the dip where the CO (1–0) temperature is at a minimum. Our conclusions will not be affected by small changes in the exact range of integration.

The mean integrated intensity and the standard deviation for the different groups in each cloud are tabulated in Table 5. The (1–0) intensities are similar for clumps 1–4 in G216−2.5 and group 3 (clumps 12–24) in the RMC, but the average (3–2) emission is about twice as great in the latter. We conclude that the clumps in the RMC have a greater fraction of hot, dense gas that can excite CO (3–2) emission than do clumps of similar mass in G216−2.5. There is also a trend with clump mass in each cloud: the (3–2)/(1–0) intensity ratio increases with clump mass. That is, clumps 12 and 14 in G216−2.5 have the lowest ratio, and in the RMC, group 1 (the star-forming clumps) has a higher ratio than group 2, which in turn has a higher ratio than group 3, the set with the lowest average mass.

Table 5 also shows that the variation in the integrated intensities and their ratio is substantially greater in the RMC. This reflects the star formation activity in the cloud, and perhaps, since those clumps without *IRAS* sources are also widely scattered in the plot, the effect of the OB association, NGC 2244, at the center of the Rosette Nebula. As in Paper II, we have looked for a correlation of properties with distance from the cluster and have found a marginal (but not statistically significant) trend for the (3–2) to (1–0) integrated intensity ratio to increase with proximity to the OB association.

The variation of (3–2)/(1–0) line temperature ratio from line center to line wing also shows a qualitatively different behavior in the two clouds (Figs. 6 and 8). In G216−2.5 clumps, the ratio tends to peak at line center and decrease toward the line wings. The signal-to-noise ratio is somewhat worse in the RMC clumps, but it can be seen that the line ratio tends to increase toward the line wings. The reason behind this effect is demonstrated in Figure 19, which plots the (3–2) line width against the (1–0) line width for clumps in each cloud. Generally, $\Delta v_{CO\,(3-2)}/\Delta v_{CO\,(1-0)} > 1$ in the RMC, and <1 in G216−2.5. This results in the observed behavior in the variation of (3–2) to (1–0) line temperature ratio with velocity in the two clouds.

The greater (3–2) to (1–0) line width ratio in the RMC cannot be due to optical depth broadening, since that would require a greater optical depth in the (3–2) line than in the (1–0) line. But since the (1–0) line is already saturated, this would imply that the (3–2) and (1–0) line temperatures should be equal, contrary to what is observed. The higher ratios of (3–2) to (1–0) emission and line widths in the RMC, therefore, are most likely due to the effect of heating sources (both internal and external) in the cloud and, by extension, the smaller (3–2) to (1–0) emission and line width ratios in G216−2.5 are due to the relative absence of heat sources.

4.2. *LVG Analysis*

The temperatures and temperature ratios of the (3–2), (2–1), and (1–0) transitions of CO can be used to constrain volume densities and kinetic temperatures. Here we use the LVG approximation to the radiative transfer (Goldreich & Kwan 1974; Scoville & Solomon 1974). This method assumes that there is a sufficient variation in the velocity of

TABLE 5

CO INTEGRATED INTENSITIES

	$W_{CO\,(1-0)}$		$W_{CO\,(3-2)}$		(3–2)/(1–0) RATIO	
CLUMP	μ	σ	μ	σ	μ	σ
G216−2.5, all clumps ……	29.6	8.8	8.5	4.0	0.27	0.08
G216−2.5 clumps 1–4……	35.5	3.0	11.1	2.1	0.31	0.07
RMC clumps 12–24………	31.7	7.1	20.8	9.9	0.63	0.21
RMC clumps 4, 5, 6, 8……	51.7	22.7	37.2	19.5	0.70	0.11
RMC *IRAS* clumps………	72.6	27.3	77.6	34.5	1.06	0.28

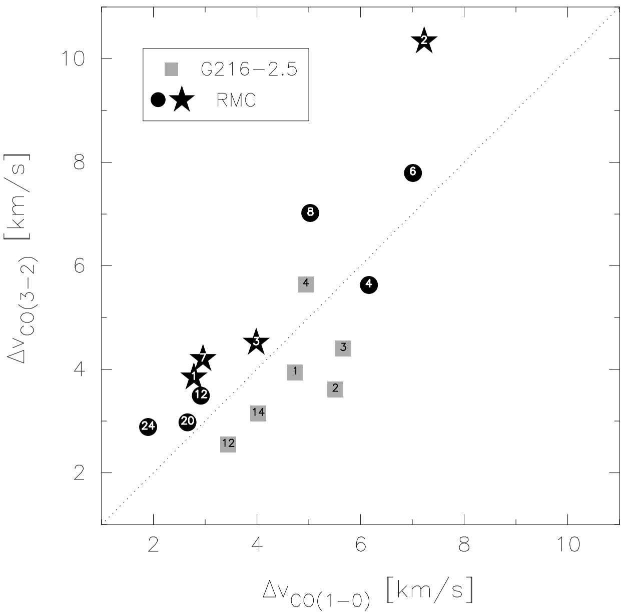

FIG. 19.—Comparison of CO (1–0) and (3–2) line widths. Symbols are the same as in Fig. 18. The dotted line corresponds to $\Delta v_{CO\,(3-2)} = \Delta v_{CO\,(1-0)}$ and shows that clumps in G216−2.5 have CO (1–0) line widths that are generally larger than clumps in the RMC but that the (3–2)/(1–0) line width ratio is smaller.

different "parcels" of gas along any particular line of sight such that there is no radiative coupling between them. This may be an overly simplistic assumption in the highly turbulent conditions within clouds, as has been noted by many authors (see, e.g., Castets et al. 1990). An additional assumption is that the excitation properties of the gas are homogeneous. Particularly in the case of the star-forming clumps in the RMC for which there are central heating sources, the reality of this assumption may also be called into question. Nevertheless, the simplicity of the LVG method is appealing, especially since the cloud geometries are not well known. It allows basic inferences to be drawn about the physical conditions of the gas and is adequate for the purposes here of a clump to clump comparison in the two clouds. It would be preferable to use less optically thick lines for such an analysis, but these are not available over such a large sample of clumps.

The LVG method determines line intensities given kinetic temperature, H_2 volume density, and CO column density. The size scale of the region over which molecules radiatively interact is set by the velocity field of the gas and is incorporated into the models by considering the column density per unit line width, $N_{CO}/\Delta v$, as the parameter of interest. For the models presented here, $N_{CO}/\Delta v$ is held constant, and line intensities are calculated for varying volume densities and kinetic temperatures.

The CO emission is very optically thick ($\tau \gtrsim 10$, judging by the strength of the ^{13}CO lines), and the column density is, therefore, poorly determined. We use ^{13}CO observations, which have a lower optical depth, to guide us; these imply peak column densities of $N_{H_2} \simeq (2\text{–}6) \times 10^{21}\,\mathrm{cm}^{-2}$ for the clumps analyzed here (Paper II). Higher column densities correlate with wider line widths, however, so the ratio of the two shows a smaller variation. For a CO to H_2 ratio of 10^{-4}, typical column densities per unit line width, $N_{CO}/\Delta v$, are $\simeq (2\text{–}4) \times 10^{17}\,\mathrm{cm}^{-2}\,\mathrm{km}^{-1}$ s. We ran three models over a range of volume densities, $n_{H_2} = 300\text{–}3000\,\mathrm{cm}^{-3}$, and kinetic temperatures, $T_{kin} = 5\text{–}50$ K, for $N_{CO}/\Delta v = 2$, 4, $6 \times 10^{17}\,\mathrm{cm}^{-2}\,\mathrm{km}^{-1}$ s.

Data points from clumps in each cloud are plotted in Figure 20. Since the CO emission in RMC clumps 2, 3, 4, and 6 is strongly self-absorbed, the line ratios are not directly interpretable in the same way as the other clumps and are not included in the plot. The (3–2) to (1–0) line temperature ratio is similar in both clouds, and the principal difference between the two is the greater (1–0) line temperature in the RMC. Typical error bars for each point are shown in the lower left-hand corner of the plot. The main source of error stems from $\sim \pm 10\%$ calibration uncertainties in the line strengths, which implies an uncertainty in the line ratio of $\sim \pm 20\%$. LVG models are overlaid for each volume density, kinetic temperature, and CO column density. Higher (3–2) to (1–0) line ratios result from both greater volume and column densities, but higher (1–0) line intensities are mostly due to greater kinetic temperatures. The conclusion is, therefore, that the volume and column densities of the emitting gas are similar in the two clouds, but the kinetic temperatures are higher in the RMC. However, the three star-forming clumps that are included in the plot do have higher (3–2)/(1–0) line ratios, indicating greater volume and/or column densities than the other RMC clumps.

CO (2–1) observations also exist for the clumps in G216−2.5, and we have compared the LVG model calculations with this data. Since the derived kinetic temperature is most sensitive to the (1–0) line temperature, there is good consistency with the (3–2) analysis. However, the near unity (2–1)/(1–0) line ratios can be matched by a range of volume and column densities and are therefore poorly determined. The most we can conclude is that, to within a factor of 2, $n_{H_2} \simeq 700\,\mathrm{cm}^{-3}$, and $T_{kin} \simeq 10$ K for clumps in G216−2.5.

4.3. CS *Comparison*

The critical density of CS (2–1) is $5 \times 10^5\,\mathrm{cm}^{-3}$, which is more than 2 orders of magnitude greater than the densities traced by CO. Dense cores are a necessary intermediate step

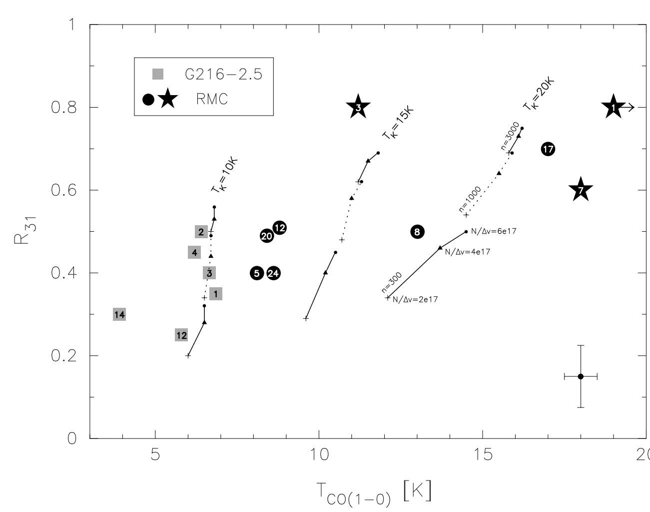

FIG. 20.—CO (3–2) to (1–0) line ratio, R_{31}, plotted against (1–0) line intensity for clumps in the two clouds. LVG models are indicated for different kinetic temperatures, volume densities, and column densities. Typical error bars for each point are shown in the lower, right-hand corner. Ratios are similar between the clumps in the two clouds, but peak (1–0) temperatures are higher in the RMC.

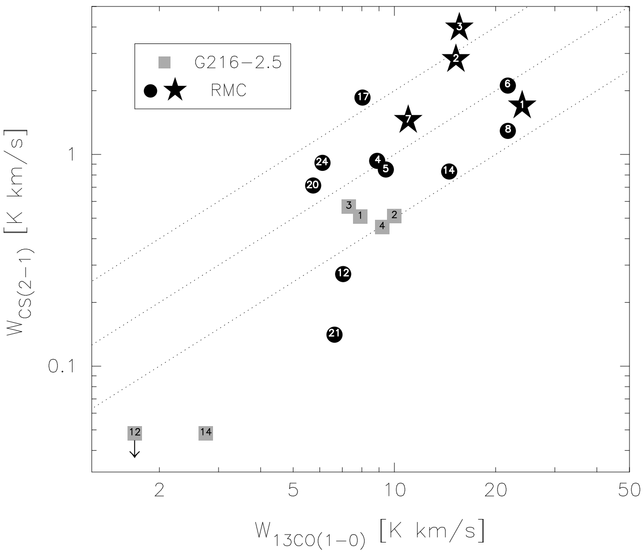

FIG. 21.—Comparison of ^{13}CO and CS peak integrated intensities. Symbols are the same as in Fig. 18. The dotted lines are at $W_{CS}/W_{CO13} = 0.2, 0.1, 0.05$. Clumps in G216−2.5 have both lower ^{13}CO and CS peak intensities than similar mass clumps in the RMC, and a lower CS to ^{13}CO ratio. Those clumps in the RMC associated with and *IRAS* source have the highest average CS intensity and CS/^{13}CO ratio.

as a clump evolves to form stars. Observations of a high-density tracer such as CS, then, may be a useful measure of a clump's propensity for star formation. Indeed, the combined molecular line–infrared study of Lada, Bally, & Stark (1991) in the OMC showed that the CS (2–1) line is an excellent signpost of the regions of star formation.

Figures 9 and 10 show that, to within a factor of 2, the CS integrated intensity of the majority of clumps in both clouds is an order of magnitude weaker than ^{13}CO. Such a low CS line strength shows that there is relatively little high-density gas, $n_{H_2} \simeq 10^5$ cm^{-3}, in either cloud. With just one transition observed, it is not possible to determine the excitation conditions of the CS-emitting gas. We have simply compared the integrated intensity of CS with ^{13}CO in Figure 21. As for the CO comparison, there is considerable scatter in the RMC clumps that is reflective of its more dynamic state. Table 6 shows that the average ratio of CS to ^{13}CO integrated intensities is higher for group 3 (clumps 12–24) in the RMC than clumps 1–4 in G216−2.5. This is suggestive of a deficiency of dense gas in G216−2.5, but it is not possible, from the data alone, to distinguish it from relative abundance variations between the two clouds. For instance, Bergin et al. (1997) show that the CS abundance within a cloud is sensitive to the gas-phase [C]/[O] ratio and tends to decrease as the (chemical) age of the gas increases.

TABLE 6

CS TO ^{13}CO COMPARISON

Clump	W_{CS}/W_{13CO} μ	W_{CS}/W_{13CO} σ	$\Delta V_{CS}/\Delta V_{13CO}$ μ	$\Delta V_{CS}/\Delta V_{13CO}$ σ
G216−2.5, all clumps	0.05	0.02	0.71	0.14
G216−2.5 clumps 1–4......	0.06	0.01	0.76	0.09
RMC clumps 12–24.........	0.10	0.07	0.84	0.09
RMC clumps 4,5,6,8	0.09	0.02	0.84	0.06
RMC *IRAS* clumps	0.16	0.07	1.01	0.11

A possibly less ambiguous comparison can be made within a cloud: the ratio is higher for those clumps (1, 2, 3, and 7) in the RMC that contain embedded *IRAS* sources than for clumps 4, 5, 6, and 8 that are of only slightly lower mass but do not contain any *IRAS* sources. The chemical models of Bergin et al. (1997) indicate that the CS abundance decreases in regions of enhanced UV flux, and therefore the greater relative CS intensities in the star-forming clumps cannot be explained by the effect of radiation from the embedded stars.

We have also compared CS and ^{13}CO line widths in Figure 22 and Table 6. The advantage of this comparison is that it is independent of chemical abundance. In both clouds, CS and ^{13}CO line widths increase in unison, but the CS line width is somewhat narrower than the ^{13}CO line width. This is to be expected if the CS emission arises from denser gas occupying a smaller volume and therefore having a smaller velocity dispersion. Clumps 12–24 in the RMC have marginally higher CS to ^{13}CO line width ratios than clumps 1–4 in G216−2.5. If the size–line width relation is the same for the two clouds, this implies that the CS-emitting gas occupies a smaller relative region in G216−2.5.

It is clear from Figure 22 that the star-forming clumps in the RMC have the highest CS to ^{13}CO line width ratio. Indeed, the biggest difference in Table 6, either in integrated intensity ratio or line width ratio, is between groups 1 and 2 in the RMC. The ratios are very similar for groups 2 and 3, despite the large difference in average clump mass between the two. The most significant change occurs in the star-forming clumps, and we conclude, as did Lada et al. (1991) for the OMC, that the contrast in emission between sites where stars do and do not form is greater in CS than in ^{13}CO.

4.4. *Clump Profile Comparison*

The velocity-integrated ^{13}CO maps of clump 1 in G216−2.5 (Fig. 11) and clump 2 in the RMC (Fig. 15) show

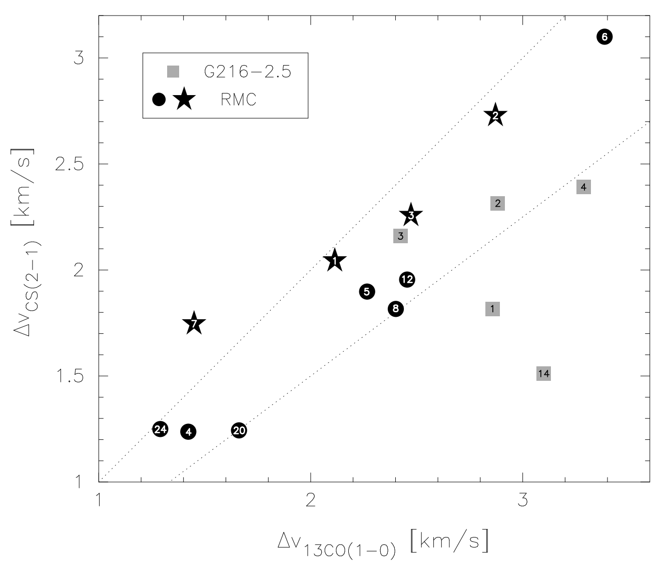

FIG. 22.—Comparison of ^{13}CO and CS FWHM line widths. Symbols are the same as in Fig. 18. The two dotted lines correspond to $\Delta v_{CS}/\Delta v_{13CO} = 1$ and 0.75. Clump line widths in G216−2.5 are relatively large, but the CS/^{13}CO line width ratio is marginally less than the ratio for clumps in the RMC. Again, those clumps in the RMC that are associated with *IRAS* sources lie on the extreme of the population, possessing the highest CS to ^{13}CO line width ratio.

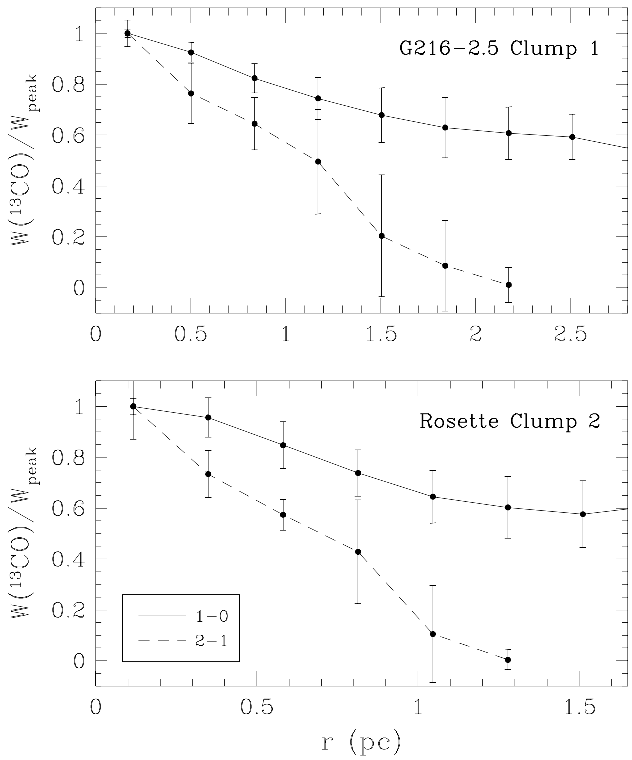

FIG. 23.—Radial profile of ^{13}CO (1–0) and (2–1) integrated intensity in G216−2.5 clump 1 and RMC clump 2. The mean and standard deviation of the integrated intensity, relative to the central peak, are shown for each radial bin. Note that the abscissa scale is different for the two clumps, and therefore that RMC clump 2 has steeper (1–0) and (2–1) profiles, but that the relative rate at which they decline is the same in the two clumps.

that the (2–1) emission is more highly concentrated than the (1–0) emission. To quantitatively compare the distributions in the two clumps, we calculated radial profiles in the same manner as described in Paper II. Annuli were defined around the center of emission, and the mean and standard deviation of integrated intensity were calculated at radial bins. The results for each clump in each line are plotted in Figure 23.

The axes in this figure are linear, but the radial ranges are different and chosen to highlight the remarkable similarity in profiles for the two clumps. Over the limited dynamic range available, the profiles can be approximated by a linear decrease, $N(r)/N_{peak} = 1 - r/r_0$, and we have tabulated the best-fit gradients, $-1/r_0$, (restricted to $r < 2.2$ pc in G216−2.5 and $r < 1.3$ pc in the RMC) for each clump and each line in Table 7. In each clump, the (2–1) profile is steeper than the (1–0) profile. However, the rate at which the (2–1) emission declines with respect to the (1–0) emission, i.e., the ratio of the (2–1) to (1–0) gradient, is the same in both clumps (third column of Table 7). That is, the main difference between the two clumps is their size: the G216−2.5 clump is a "puffed up" version of the RMC clump, and the physical reason for the steeper (2–1) to (1–0) profiles, therefore, may be the same for each clump. Williams (1995) arrived at a similar conclusion regarding the structural difference between large-scale ^{13}CO maps of each cloud. At the density levels, $n_{H_2} \sim 10^3$ cm^{-3}, that these ^{13}CO observations are sensitive to, clump and cloud differences appear to be predominantly nothing more than a change in scale.

If we now take scale into account, we see from the smaller radial range in the lower panel (RMC clump 2) that the profiles are steeper than G216−2.5 clump 1. The size, r_0, of the clumps [whether measured in the (1–0) or (2–1) line] is inversely proportional to the gradient and is a factor of $0.34/0.20 = 0.79/0.47 = 1.7$ higher in G216−2.5 clump 1. On the other hand, the mass, M, of RMC clump 2 is a factor of 4.8 greater than G216−2.5 clump 1, which implies that the peak column density, $N_{peak} \sim M/r_0^2$, is a factor of 14 greater and that the average density, $\sim M/r_0^3$, is a factor of 24 greater in the RMC clump. Since the LVG analysis implied that the typical density of the CO-emitting gas is similar in the two clouds, the filling factor of this gas must be a greater by the same factor of 24 in RMC clump 2 than in G216−2.5 clump 1.

4.5. *Global Comparison*

Star formation is clearly much more developed in the RMC than in G216−2.5 based on the infrared luminosity of the two clouds (Blitz 1987). Although it is tempting to suggest that G216−2.5 is a cloud so young that it has not yet had time to form stars (Maddalena & Thaddeus 1985), an apparent physical association of the H II region S287 with the GMC (Williams & Maddalena 1996) suggests that G216−2.5 may have already gone through at least one episode of star formation (see also Lee, Snell, & Dickman 1994). The star formation efficiency of molecular clouds has long been known to be low (Zuckerman & Evans 1974), and since nearly all star formation in GMCs takes place in dense clusters (Lada et al. 1991), we infer that most of the volume of a GMC is dormant and remains that way until it is dispersed by the effects of massive star formation. G216−2.5 is unusual because the dormant portion of the cloud encompasses essentially its entire volume.

In any event, the two clouds do appear to represent two different evolutionary stages in the star formation history of a GMC. The largest and most massive clumps in G216−2.5 have properties remarkably similar to each other and to the dormant clumps in the RMC (group 3). The masses are similar (Tables 3 and 4), the densities in their ^{13}CO-emitting regions are similar (Fig. 20), their excitation conditions are similar (Figs. 18 and 20), and their dynamical state as measured by their line widths are similar (Fig. 19). The dormant clumps in the RMC manifest a greater fraction of their internal energy as gravitational energy, but even the RMC clumps are only marginally gravitationally bound. Lower mass clumps in the RMC ($M \lesssim 200\ M_\odot$) have as little gravitational energy as the most massive G216−2.5 clumps

TABLE 7

CLUMP PROFILE GRADIENTS

Clump	^{13}CO (1–0) Gradient	^{13}CO (2–1) Gradient	(2–1)/(1–0) Ratio
G216−2.5 clump 1......	−0.20	−0.47	2.35
RMC clump 2	−0.34	−0.79	2.32

(Paper II) and in both cases are probably pressure bound (Blitz 1987; Bertoldi & McKee 1992). The similarity in the slope of the clump mass spectrum between the two clouds (Paper I) suggests that all of the dormant clumps in both clouds are likely to have similar properties. In fact, the largest difference between the dormant clumps in the RMC and the most massive clumps in G216−2.5 is that the former are somewhat warmer, very likely owing to the ambient heating sources from the massive star formation in the RMC.

It seems reasonable that the three groups of clumps in the RMC represent an evolutionary sequence: dormant → incipient star forming → star forming. If so, the present observations suggest how the physical conditions change as we proceed along the evolutionary path. The similarity of the dormant clumps both within a cloud and between the two GMCs suggests that all clumps are formed with more or less the same initial conditions but differ only in mass. Apparently all large clumps with $M \gtrsim 100\ M_\odot$ have similar densities in their ^{13}CO-emitting regions, regardless of where they are on the evolutionary sequence. The clumps in all three groups in the RMC have similar density profiles (Fig. 22 of Paper II) and differ from those in G216−2.5 only in scale (Fig. 23). We discussed in Paper II how agglomeration could increase clump masses while preserving the slope of the mass spectrum. The results here suggest that there is a mass threshold, $M \sim 800\ M_\odot$, above which dormant clumps progress to the incipient star-forming phase. As this happens, the density profiles become steeper but maintain their same relative shape (Fig. 23), implying that the volume-filling fraction of the ^{13}CO-emitting gas goes up considerably (and thus the volume-averaged H_2 density within a clump; see also § 4.4), and the clumps become more tightly bound and approach virialization. It is probably at this stage that the individual subcondensations that are to become single stars and binaries form or become distinct entities, at a scale too fine to be resolved by our observations.

When the central densities reach a high enough value, conditions in the incipient star-forming clumps are such that subcondensations within them begin to form stars. This results in heating of these clumps, raising the CO (3–2)/(1–0) ratio (Figs. 6, 8, and 18). Once massive stars form as in the RMC, the local UV radiation field is raised, and there may be sufficient heating of the entire molecular cloud to account for the higher temperatures in the dormant clumps in the RMC (Schneider, Stutzki, & Winnewisser 1998).

This outline also suggests that the dormant clumps in the RMC are more evolved than the dormant clumps of similar mass in G216−2.5. The former show higher CS to ^{13}CO intensities (Figs. 9 and 10), suggesting more dense gas in the latter, steeper radial density profiles and a greater degree of gravitational boundness. There may be secondary parameters, therefore, in addition to mass that drive the evolution of a clump (e.g., the proximity to regions of massive star formation; Elmegreen & Lada 1977).

The paucity of clouds such as G216−2.5 suggests that the evolution from the dormant clump phase in a molecular cloud to the star-forming phase must occur quite rapidly, on timescales less than a few times 10^6 yr, judging from cloud lifetimes of order 3×10^7 yr (Blitz & Shu 1980) and the low fraction of quiescent GMCs (Williams & McKee 1997). In the RMC, about 10% of the mass of the cloud is in active, star-forming clumps (Paper II). Because of the similar masses of the incipient and star-forming clumps, the mass fraction of incipient star-forming clumps is similar, also about 10% by mass. Therefore, a substantial fraction, ∼80%, of the mass of a cloud is locked up in dormant clumps, and the evolutionary process from dormant to star forming, though rapid for the cloud as a whole, is relatively inefficient for any one clump. The total star-forming efficiency of molecular clouds may be kept low because the conditions for forming incipient star-forming clumps occur only in a small volume of the cloud as a whole. Once one of these clumps form, however, the subsequent evolution is evidently quite rapid. It may also be true that many of the star-forming clumps also have a relatively low star formation efficiency, as suggested by the observations of Phelps & Lada (1997). Their data imply that the stars currently forming in the star-forming clumps in the RMC are only a small fraction of the mass (and volume) of these clumps. Unless these clumps ultimately turn a much larger fraction of their mass into stars, it is unclear whether the inefficiency of the star formation process is due to the rate of formation of star-forming clumps or to the inefficiency with which star formation takes place in the active star-forming gas.

5. SUMMARY

In this paper, we have presented and compared observations of $J > 1$ transitions of CO and CS (2–1) in the RMC and G216−2.5. We list the following main results:

1. The CO (2–1) to CO (1–0) ratio anticorrelates with the CO (1–0) intensity in G216−2.5, increasing toward the clump edges. This is opposite to what is seen in the OMC by Sakamoto et al. (1994) and is interpreted as resulting from low-density gas that is becoming optically thin in the (2–1) line.

2. Clumps 1–4 in G216−2.5 possess remarkably uniform excitation conditions. CO and ^{13}CO line profiles are strikingly similar and indicate very uniform kinetic temperatures and densities.

3. There is a much wider variation of excitation conditions in the clumps in the RMC. This is true even when considering a subset of just the most massive ones. This range of physical properties reflects the active star-forming nature of the RMC.

4. The integrated CO (3–2) intensity is a factor of 2 weaker for the most massive clumps in G216−2.5 than similar mass clumps in the RMC, indicating a relative deficiency of warm, dense gas in the former.

5. The clumps in the RMC with embedded *IRAS* sources have higher CO (3–2) intensities and (3–2)/(1–0) ratios than other clumps in the RMC. These clumps have the greatest amount of warm and dense gas.

6. Clumps in G216−2.5 have large CO (1–0) line widths, but relatively small CO (3–2) line widths. The (3–2)/(1–0) line width ratio is less than one for most clumps in G216−2.5 but exceeds one for almost all clumps in the RMC (star forming or not).

7. Clumps in each cloud have similar CO (3–2)/(1–0) line temperature ratios, ≃0.4–0.5, but RMC clumps have greater CO (1–0) peak brightness temperatures. To the extent that LVG models can reliably model such saturated lines, we find typical volume densities of $n_{H_2} \simeq 10^3$ cm^{-3} for the emitting gas in both clouds. Kinetic temperatures are less than 10 K for all clumps in G216−2.5 and $\gtrsim 12$ K for all the observed clumps in the RMC.

8. The RMC clumps with embedded *IRAS* sources have higher (3–2)/(1–0) line temperature ratios, indicating higher volume and/or column densities than other clumps in the cloud.

9. In both clouds, CS (2–1) integrated intensities are generally 1 order of magnitude weaker than ^{13}CO (1–0) integrated intensities, indicating that there is little gas in either cloud at densities of $n_{H_2} \gtrsim 10^5 cm^{-3}$. The ratio of CS to ^{13}CO intensities is somewhat weaker in G216−2.5 than clumps of similar mass in the RMC and highest of all in the star-forming RMC clumps.

10. The ratio of CS (2–1) to ^{13}CO (1–0) line widths is slightly less for clumps in G216−2.5 than clumps of similar mass in the RMC. Again, those clumps in the RMC with embedded *IRAS* sources possess the highest ratios of all.

11. Radial profiles of ^{13}CO (2–1) decline more rapidly than ^{13}CO (1–0) in RMC clump 2 and G216−2.5 clump 1. For each transition, the profiles are steeper in the RMC clump. However, the relative rate of decline of the (2–1) with respect to the (1–0) emission is the same in the two clumps, as if the only difference between the two was the size scale of the two clumps and not their structure.

12. The smaller size, but greater mass, of RMC clump 2 compared to G216−2.5 clump 1 implies a much higher peak column density and average volume density in the former. Taken together with the LVG result that the volume density of emitting gas is similar in the two clouds, this means that the filling fraction of emitting gas is more than an order of magnitude greater in the RMC clump.

G216−2.5 and the RMC have radically different star formation rates. The results here, which compare observations of individual clumps in many lines, complement the results of Paper I, which compare the collective properties of clumps observed in a single line. In that study, the scaling laws between clump mass, peak temperature, size, line width, and the ratio of virial to LTE mass were found to have similar power-law indices but different offsets for each cloud. The conclusion was that at the densities, $n_{H_2} \simeq 10^3$ cm^{-3}, traced by the ^{13}CO (1–0) line, the clump ensembles (i.e., clouds) evolve globally rather than on a individual, clump by clump basis.

Moreover, Paper II showed that it was not possible to distinguish those clumps with embedded *IRAS* sources in the RMC from similar mass clumps in the same cloud that were not star forming from the ^{13}CO (1–0) maps alone. Here, however, the $J > 1$ CO and CS observations show not only that clumps in the RMC are hotter and also have more dense CS-emitting gas than G216−2.5 but also distinguish the star-forming clumps in the RMC from the other clumps in the cloud without embedded *IRAS* sources. Therefore, it appears that at these higher densities, $n_{H_2} \gtrsim 10^5$ cm^{-3}, clumps do evolve independently of each other.

Finally, we note that clumps 6 and 8 in the RMC stand out as excellent candidates for sites of future star formation in this cloud. Both are gravitationally bound, massive, and situated toward the cloud center in a region of high clump density, yet possess no infrared sources (Phelps & Lada 1997) or apparent CO outflows. However, they have high CO (3–2) to (1–0) intensity and line width ratios and high ^{13}CO intensities that place them closer to the star-forming clumps 1, 2, 3, and 7 than the non–star-forming clumps in Figures 18, 19, and 21. We suggest, therefore, that these two clumps are the most likely regions where future star formation will occur in the RMC, and as such, they provide an opportunity to study the undisturbed initial conditions of a star-forming region.

J. P. W. thanks the Harvard-Smithsonian Center for Astrophysics for fellowship support. L. B. is supported by funding from the NSF and NASA. We would like to thank L. Nyman at SEST, N. Schneider and R. Simon at Gornergrat, and P. Jewell at NRAO for their help and advice concerning their respective telescopes. Conversations with L. Mundy are gratefully acknowledged.

REFERENCES

Bergin, E. A., Goldsmith, P. F., Snell, R. L., & Langer, W. D. 1997, ApJ, 482, 285
Bertoldi, F., & McKee, C. F. 1992, ApJ, 395, 140
Blitz, L. 1987, in Physical Processes in Interstellar Clouds, ed. G. E. Morfill & M. Scholer (Dordrecht: Reidel), 35
———. 1990, in ASP Conf. Proc. 12, The Evolution of the Interstellar Medium, ed. L. Blitz (San Fransisco: ASP), 273
———. 1993, in Protostars and Planets III, ed. E. H. Levy & J. I. Lunine (Tuscon: Univ. of Arizona Press), 125
Blitz, L., & Shu, F. H. 1980, ApJ, 238, 148
Blitz, L., & Stark, A. A. 1986, ApJ, 300, L89
Blitz, L., & Thaddeus, P. 1980, ApJ, 241, 676
Booth, R. S., et al. 1989, A&A, 216, 315
Carpenter, J. M., Snell, R. L., & Schloerb, F. P. 1990, ApJ, 362, 147
Castets, A., Duvert, G., Dutrey, A., Bally, J., Langer, W. D., & Wilson, R. W. 1990, A&A, 234, 469
Cohen, M. 1973, ApJ, 185, L75
Cox, P., Deharveng, L., & Leene, A. 1991, A&A, 230, 171
Elmegreen, B. G., & Lada, C. J. 1977, ApJ, 214, 725
Goldreich, P., & Kwan, J. 1974, ApJ, 189, 441
Kutner, M. L., & Ulich, B. L. 1981, ApJ, 250, 341
Lada, C. J., & Gautier, T. N. 1982, ApJ, 261, 161
Lada, E. A., Bally, J., & Stark, A. A. 1991, ApJ, 368, 432
Lee, Y., Snell, R. L., & Dickman, R. L. 1994, ApJ, 432, 167
———. 1996, ApJ, 472, 275
Maddalena, R., & Thaddeus, P. 1985, ApJ, 294, 231
Mooney, T. J., & Solomon, P. M. 1988, ApJ, 334, L51
Phelps, R., & Lada, E. A. 1997, ApJ, 477, 176
Sakamoto, S., Hayashi, M., Hasegawa, T., Handa, T., & Oka, T. 1994, ApJ, 425, 641
Schneider, N., Stutzki, J., & Winnewisser, G. 1998, A&A, submitted
Scoville, N. Z., & Good, J. C. 1989, ApJ, 339, 149
Scoville, N. Z., & Solomon, P. M. 1974, ApJ, 187, L67
Williams, J. P. 1995, PhD thesis, University of California, Berkeley
Williams, J. P., & Blitz, L. 1993, ApJ, 405, L75
Williams, J. P., Blitz, L., & Stark, A. A. 1995, ApJ, 451, 252 (Paper II)
Williams, J. P., de Geus, E. J., & Blitz, L. 1994, ApJ, 428, 693 (Paper I)
Williams, J. P., & Maddalena, R. J. 1996, ApJ, 464, 247
Williams, J. P., & McKee, C. F. 1997, ApJ, 476, 166
Zuckerman, B., & Evans, N. J. 1974, ApJ, 192, L149